ADVANCED HEALTHCARE MATERIALS
www.advhealthmat.de

Incorporating Stem Cell-Derived Small Extracellular Vesicles into a Multifunctional OHAMA-EPL Hydrogel Spray for Rapid Healing of Infected Skin Wounds

Mingzhu He, Yongchun Wei, Xujing Chen, Jingqi Li, Jingjing Kang, Bowei Li, Dingbin Liu, and Hong Cai**

Wound healing is a significant clinical concern that can be hindered by excessive inflammation, infection, and insufficient regeneration. Small extracellular vesicles (sEVs) derived from stem cells have been extensively studied for wound healing, but their efficient delivery and controllable release in the targeted tissues remain a technical challenge. A stem cell-derived sEVs incorporated dual-network hydrogel spray system is prepared for the rapid healing of infected full-thickness skin wounds for the first time. This multifunctional hydrogel spray, which is composed of methacrylate-modified oxidative hyaluronic acid (OHAMA) and poly-ϵ-L-lysine (EPL), possessed self-healing, injectable, adhesive, antibacterial, and pH-responsive degradation properties. These properties are crucial for facilitating the entire healing process. The efficacy of the sEVs-loaded hydrogel spray is evaluated at cellular and animal levels. In vitro analyses demonstrated the sEVs' specific functions in promoting cell proliferation, migration, and angiogenesis, working in concert with the hydrogels to augment these effects. In vivo, the spray exhibited rapid wound closure, with a 92.63% closure rate after 14 days of treatment. Furthermore, the spray also showed excellent angiogenesis and matrix deposition promotion, as well as inflammation amelioration in the treatment of infected full-thickness wounds. This study provides new insights into the development of sEVs dosage forms for the rapid healing of acute infected wounds.

1. Introduction

As the natural barrier of the human body, skin provides mechanical protection, prevents water loss, and plays crucial roles in temperature regulation, stimuli-sensing, and immune regulation. Skin is prone to damage in daily life because of its continual exposure to the outside environment. Normal wound healing encompasses four stages: hemostasis, inflammation, proliferation, and remodeling. This process involves a complex interplay of various cell types, cytokines, and the extracellular matrix (ECM).[1] Minor skin wounds typically heal within days, while larger injuries from accidents or surgical procedures may require several weeks to heal.[2] However, excessive inflammation or inadequate tissue regeneration, frequently induced by infections or poor treatment, may result in hypertrophic scars or even life-threatening sepsis.[2] These complications pose major threats to individuals' physical and mental health and present ongoing challenges for healthcare professionals.[3] Therefore, developing strategies to promote rapid wound closure while preventing infections and promoting tissue regeneration is crucial for advancing the next generation of wound dressings.

Mesenchymal stem cells (MSCs) are adult stem cells with immunomodulatory properties, self-renewal capabilities, long-term proliferation, and differentiation potential in vitro, which endow the cells with latent capacity to promote tissue regeneration.[3b,4] However, challenges remain in biological activity retention, substance

M. He, X. Chen, H. Cai
Air Force Clinical College
Anhui Medical University
Beijing 100142, P. R. China
E-mail: ch1031@163.com
M. He, X. Chen, H. Cai
The Fifth School of Clinical Medicine
Anhui Medical University
Hefei 230032, P. R. China
M. He, X. Chen, B. Li, H. Cai
Department of Dermatology
Air Force Medical Center, PLA
Beijing 100142, P. R. China
Y. Wei, J. Li, J. Kang, D. Liu
State Key Laboratory of Medicinal Chemical Biology
Tianjin Key Laboratory of Molecular Recognition and Biosensing
Frontiers Science Center for New Organic Matter
College of Chemistry
Nankai University
Tianjin 300071, P. R. China
E-mail: liudb@nankai.edu.cn
The ORCID identification number(s) for the author(s) of this article can be found under https://doi.org/10.1002/adhm.202404147

DOI: 10.1002/adhm.202404147

quantification, delivery, and oncogenicity in clinical therapy.[5] Research indicates that the regenerative therapeutic effects of MSCs are primarily mediated through paracrine mechanisms.[4a,6] As the key components of paracrine actions, sEVs—biosynthesized through lipid bilayer encapsulation of various functional biological components (including lipids, proteins, and nucleic acids) during membrane transport—retain the therapeutic properties of their maternal cells but offer enhanced stability, targeted delivery capability, and better distribution in vivo.[7] Meanwhile, they avoid the immune rejection and tumorigenicity of traditional cell therapy.[8] Above all, MSC-derived sEVs could replace MSC therapy to regulate intercellular communications, transfer bioactive substances to recipient cells, and thus facilitate the functional enhancement of various skin cells involved in wound healing.

Currently, the most prevalent method for delivering sEVs is injection, which curtails the therapeutic potential of sEVs due to their invasiveness and rapid clearance, particularly in the treatment of full-thickness skin wounds that require prolonged and continuous administration.[9] Many studies have highlighted the potential of multifunctional hydrogels as slow-release carriers for drug delivery. To fulfill the diverse needs of different wound types and respective treatment scenarios, various dosage forms of hydrogel dressings have been developed, including prefabricated hydrogel patches, microneedles, and in situ forming hydrogels.[10] In contrast to prefabricated hydrogels, in situ forming hydrogels boast the advantages of portability, non-invasiveness, and precision in sEVs delivery.[11] Among them, sprayable hydrogels excel in their adaptability to irregularly-shaped wounds, providing uniform coverage to the wound areas.[12] Meanwhile, the fast-spraying capability of hydrogel facilitates an immediate and cohesive interface with surrounding tissues, thereby establishing a physical barrier to inhibit bacterial infection. In addition, sprayable hydrogels can be a carrier of homogeneous sEVs suspension with a stable and uniform gel layer formation to improve drug delivery efficiency. So far, there is a dearth of research on the utilization of multifunctional hydrogel spray loaded with sEVs for the treatment of skin wounds.

The performance of hydrogels is primarily determined by the inherent characteristics of their constituent materials. The solubility of raw materials and mechanical strength post-gelation are crucial for the applicability and performance of sprayable hydrogels in wound management. In the selection of hydrogel materials, we have specifically focused on modified hyaluronic acid (HA) and poly-ϵ-L-lysine (EPL) due to their unique properties and promising applications. HA, renowned for its wide-spread presence in extracellular matrices, connective and dermal tissues, is highly valued in biomedicine and tissue engineering for its excellent biocompatibility and non-immunogenicity.[11,13] As an antimicrobial peptide, EPL is favored in antimicrobial research due to its broad-spectrum antimicrobial activity and minimal cytotoxicity.[14] These properties make HA and EPL optimal candidates for creating multifunctional hydrogels intended for drug delivery applications and wound healing processes. Currently, hydrogels composed of oxidative hyaluronic acid (OHA) and EPL have been demonstrated to be effective drug delivery systems in wound treatment applications.[15] Nevertheless, the poor mechanical strength of hydrogels formed via dynamic Schiff base bonds, coupled with the low solubility of OHA, presents substantial obstacles to developing a sprayable hydrogel platform for sEVs delivery.

In this study, we proposed an MSC sEVs-incorporated multifunctional sprayable hydrogel system for the rapid healing of acute infected wounds. The hydrogel scaffold is composed of EPL and methacrylate-modified OHA (OHAMA), and is named OE-Gel. OHAMA has a higher solubility than OHA, which is conducive to the uniform distribution of sEVs and spray application. In addition, OHAMA can form photo-crosslinking bonds, thereby enhancing the structural stability of the hydrogel. The OE-Gel spray exhibits properties including self-healing, adhesion, antibacterial capabilities, and pH-responsive degradation ability, thereby serving as an effective platform for sophisticated wound management and sEVs delivery (**Figure 1a**). MSC-derived sEVs were encapsulated into the OE-Gel to yield OE-sEVs-Gel, which significantly promotes cell proliferation, migration, and tube formation. The sustained slow release of sEVs from OE-sEVs-Gel was further evaluated in vitro. Therewith, we validated the efficacy of this spray in treating wounds using a mouse full-thickness infected wound model (Figure 1b). The results indicated that the spray effectively combated bacterial infection, alleviated inflammation, and enhanced skin regeneration, which was primarily due to the ability of OE-sEVs-Gel to sustain the slow release of sEVs without affecting their bioactivity and function. Additionally, we explored the impact of the released sEVs on wound angiogenesis and scarring, revealing their promising therapeutic potential to facilitate optimal wound healing.

2. Results

2.1. Synthesis and Characterization of the Hydrogels

HA derivatives are widely distributed in extracellular, connective, and dermal tissues, and are known for their excellent biocompatibility and non-immunogenicity.[16] Furthermore, the high moisturizing, viscoelastic, and anti-inflammatory properties of HA provide optimal wound healing environments and effectively promote tissue regeneration. In this study, we chose OHAMA to construct the hydrogel networks since its solution is more soluble and easier to spray than HA. Following the fabrication process (Figure S1a, Supporting Information), OHAMA was successfully synthesized and characterized by FTIR and ^{1}H NMR. FTIR analysis was performed to identify the functional groups. The stretching bands at 1648.9 and 1725.5 cm^{-1} were attributed to the C═C bond from methacrylate and the C═O bond from the aldehyde group within OHAMA (**Figure 2d**). Two new peaks at 5.7 and 6.1 ppm were observed in the ^{1}H NMR spectrum of OHAMA, corresponding to protons within the C═C bond. Additionally, ^{1}H NMR spectra identified two new peaks at 4.9 and 5.0 ppm in OHAMA and OHA, respectively, attributed to semi-acetyl protons derived from the aldehyde group and the adjacent hydroxyl group (Figure 2c).[17]

Bacterial infection is the primary factor exacerbating inflammation and causing delayed healing.[18] We wanted to incorporate antibacterial units into the multi-functional hydrogels. Owing to their broad-spectrum antimicrobial activity and low cytotoxicity, antimicrobial peptides are preferred for antibacterial studies. EPL, a natural cationic polypeptide produced by

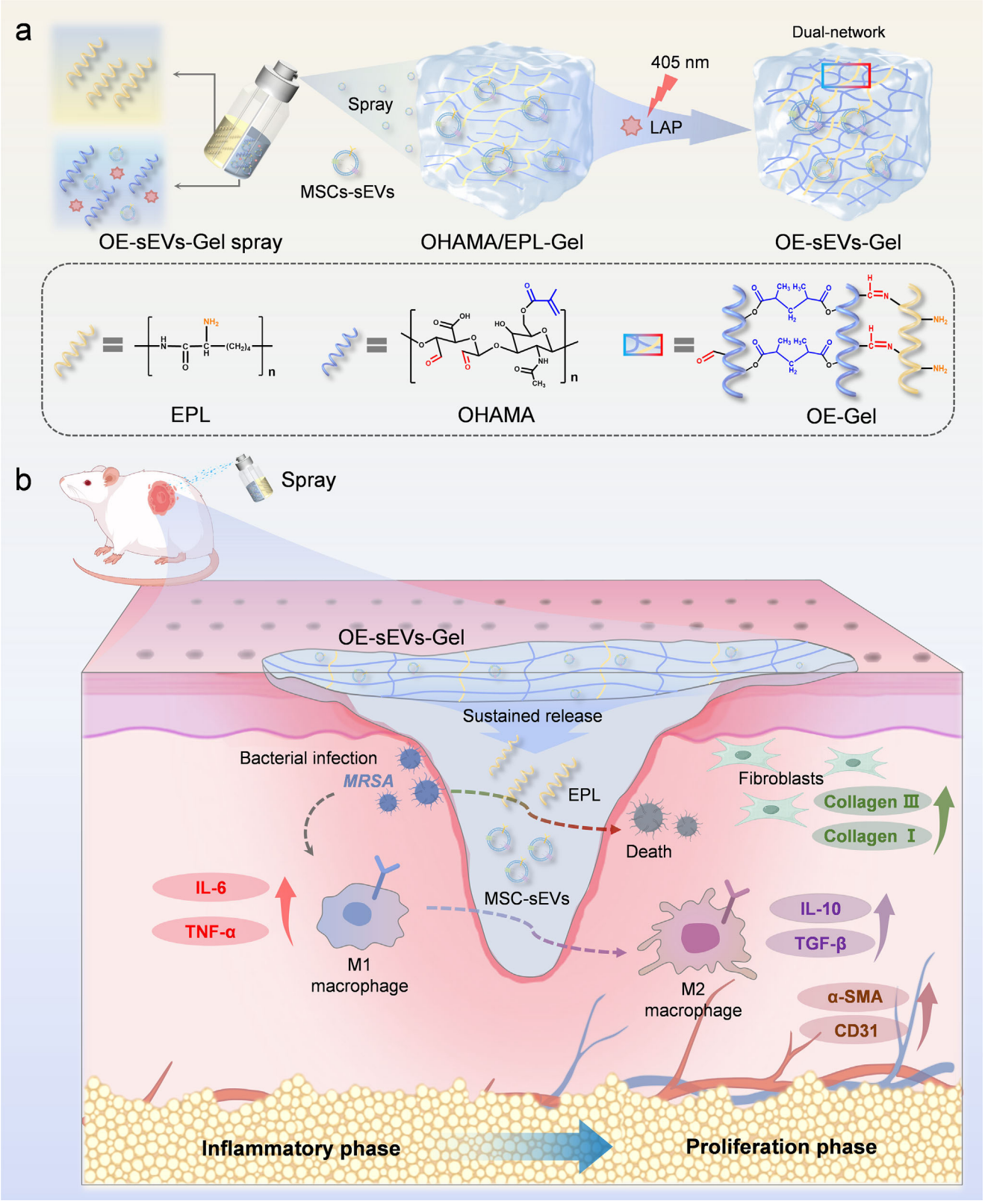

Figure 1. Schematic illustration of OE-sEVs-Gel-mediated wound healing. a) Crosslinking mechanisms and structure of OE-sEVs-Gel. b) Enhanced wound healing, achieved due to the antibacterial property, sustained sEVs delivery, anti-inflammatory effect, angiogenesis, and collagen deposition promotion programmed by OE-sEVs-Gel.

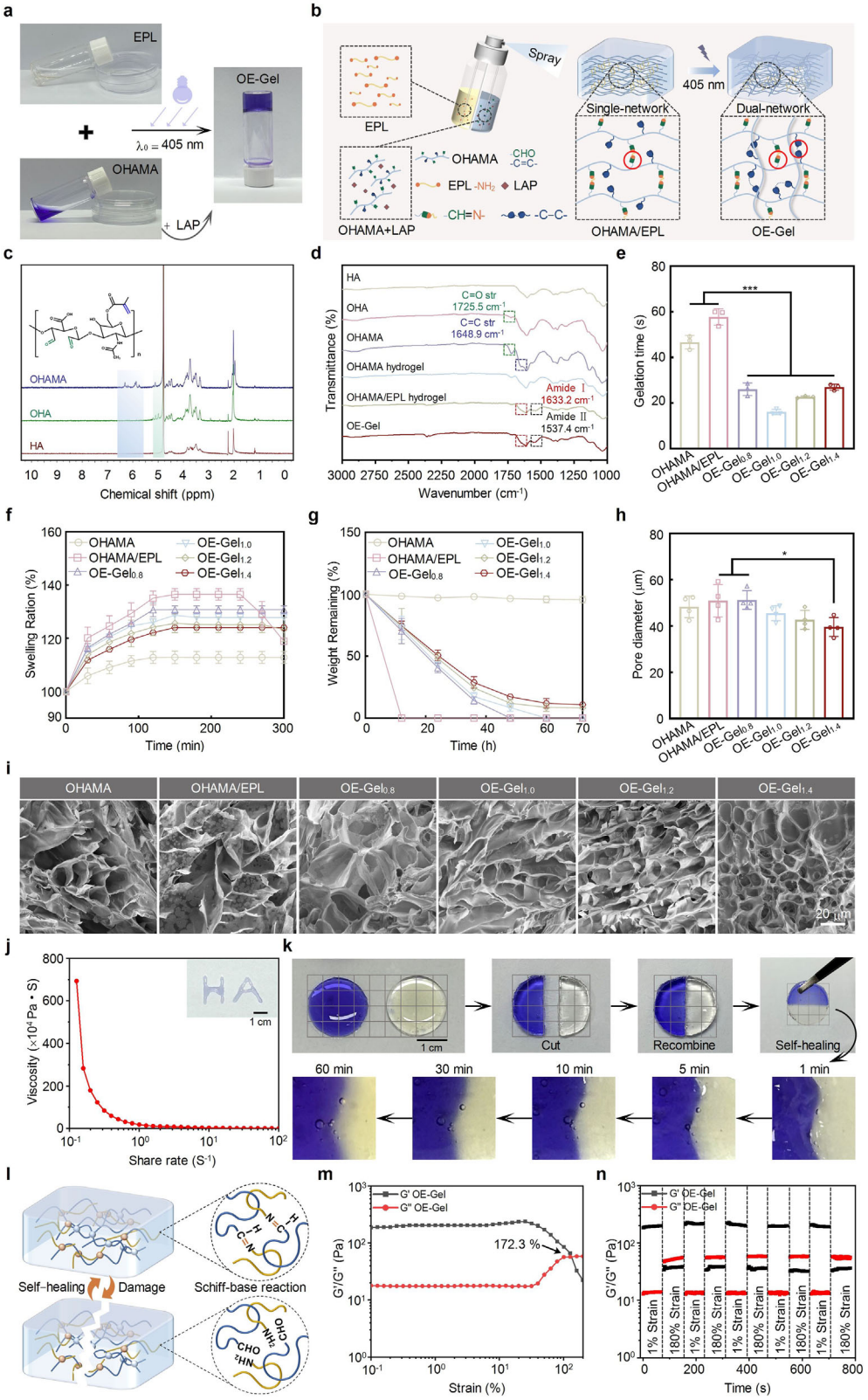

Figure 2. Synthesis and characterization of the hydrogels. a) Formation of OE-Gel. b) Schematic representation of the synthesis and chemical structure of OE-Gel. c) ^{1}H NMR spectra of HA, OHA, and OHAMA in D_2O. d) FTIR spectra of HA, OHA, OHAMA, OHAMA hydrogel, OHA/EPL hydrogel, and OE-Gel. e) Gelation time of the hydrogels. f) Swelling properties of the hydrogels in PBS at 37 °C. g) The degradation of the hydrogels in PBS at 37 °C. h) Pore sizes of the hydrogels. i) SEM images of the hydrogels. Scale bars, 20 μm. Data are means ± SD ($n = 3$). j) Shear-thinning properties of OE-Gel.

Streptomyces albus (*S. albus*), exhibits excellent biodegradability, inherent antibacterial activity, and biocompatibility.[9,12,19] Therefore, EPL was coupled with OHAMA to fabricate a dual-network hydrogel spray. To do this, OHAMA and EPL were dissolved in PBS and distilled water, respectively. Both pre-gel solutions were low-viscosity liquids, which was an important prerequisite for the materials to be sprayable (Figure S2, Supporting Information). The single-network OHAMA/EPL hydrogel was prepared via the covalent formation of Schiff-base bonds alone, whereas the dual-network OE-Gel was formed under the irradiation of 406 nm light toward OHAMA/EPL hydrogel in the presence of the photo-initiator lithium phenyl (2,4,6-trimethylbenzoyl) phosphonate (LAP). The formation of hydrogels was verified by the vial tilt method (Figure 2a), and the bonding mechanisms were illustrated (Figure 2b; Figure S1b–d, Supporting Information). Subsequent FTIR analysis of the freeze-dried hydrogels revealed that the OHAMA/EPL and OE-Gel exhibited characteristic absorption peaks of the amide bond at 1633.2 and 1537.4 cm^{-1}, corresponding to the C═O stretching vibration band (amide I) and the N-H bending vibration band (amide II), respectively (Figure 2d).[20] Conversely, these peaks were absent in the OHAMA hydrogel, which confirmed the formation of Schiff-base bonds in both OHAMA/EPL and OE-Gel.

To elucidate the hydrogel properties, we analyzed the characteristics of OHAMA hydrogel, single-network OHAMA/EPL hydrogel, and dual-network OE-Gel with different OHAMA/EPL mass ratios (R) (Table S1, Supporting Information). The hydrogels displayed were prepared and subsequently evaluated the gelation time, microscopic morphology, swelling, and degradation abilities. Gelation time analysis showed that OE-Gel, with an average gelation time of 22.98 s, gelatinized more rapidly than the single network hydrogels (Figure 2e). When R = 1.0, the gelation time of OE-Gel was slightly shorter than the other three groups (R = 0.8, 1.2, and 1.4). The difference was not statistically significant ($P > 0.05$). The SEM images demonstrated that all of the hydrogels possessed a porous structure (Figure 2i). The average pore sizes of OE-Gels were 51.23, 40.59, 42.68, and 39.56 μm, corresponding to R = 0.8, 1.0, 1.2, and 1.4 respectively (Figure 2h). The average pore diameter decreased with a higher concentration of OHAMA, which may be related to the higher proportion of photo-crosslinking bonds.

Then, we conducted a swelling assay to test the exudate absorption and moisture retention capacities of the hydrogels (Figure 2f). While all of the hydrogels showed swelling properties, the OHAMA hydrogel had the lowest swelling ratio, which suggests that its network structure is denser. In contrast, the OHAMA/EPL hydrogel exhibited the highest swelling ratio, reflecting a looser and more porous structure. The swelling ratios of the OE-Gels dropped with an increase in OHAMA concentrations; this tendency correlates positively with the increased proportion of photo-crosslinking bonds. The effective degradation ability of hydrogels can prevent further injuries associated with dressing changes and the persistence of hydrogel residues in deep wounds. Continuous monitoring revealed distinct degradation patterns of the hydrogels (Figure 2g). Owing to different bond crosslinking strengths, the degradation ratio of OHAMA hydrogel was less than 10% by day 3, whereas the degradation process of the OHAMA/EPL hydrogel was completed within 12 h. For OE-Gels, degradation ratios slowed down with higher OHAMA concentrations but still exceeded 85% within 3 d. OE-$Gel_{1.2}$ was selected for the following experiments to ensure that over 90% of the hydrogel degraded, allowing sEVs to release prior to excipient replacement, while the remaining 10% of the hydrogel protected the wound area from infection. In short, OE-Gels displayed rapid gelation, porous structure, appropriate swelling ratio, and good degradation ability, which made it an ideal sEVs-carrier dressing spray.

2.2. Characterization of the Properties of OE-Gel

A rheological experiment was performed to verify the injectability of OE-Gel. As shown in Figure 2j, the fluidity of OE-Gel is positively associated with the shear rate, implying the shear-thinning ability of the hydrogels. The injectability was further evaluated by extruding it with a syringe to write "HA". The excellent self-healing and adhesion properties make hydrogel an ideal dressing for wounds that undergo frequent stretching, as it quickly and autonomously repairs mechanical damage.[21] In addition, the self-healing capacity of hydrogel dressing is also important for its adaptability to wounds.[9] Upon reassembling the two fragmented hydrogels, we found that they fused seamlessly and supported their weight. Microscopic observations showed the migration of methyl-blue-stained hydrogel into an undyed counterpart, confirming effective self-healing (Figure 2k).

Then, we examined the self-healing behavior at the microscopic level.[22] The hydrogel structure collapsed at a strain of 172.3% (Figure 2m). In the subsequent alternate strain test, the hydrogel reverted to its original gel state after cycling between 180% and 1% strains, demonstrating resilience over five cycles (Figure 2n). The primary mechanism of self-healing in OE-Gel is attributed to Schiff-base reactions (Figure 2l). Adhesion is an indispensable property of sprayable hydrogels. As shown in Figure S3a (Supporting Information), OE-Gel adhered firmly to a human finger, maintaining contact during bending from 0° to 90°, and also showed strong adhesion to wet porcine skin (Figure S3b, Supporting Information), demonstrating its high adaptability. These properties confirm that OE-Gel is highly suitable for managing irregularly shaped wounds, resisting external physical stress, and providing protection from further infection after dressing damage under diverse conditions.[23] Hence, OE-Gel can be used as an emergency treatment for wounds in various situations.

Inset: "HA" written by the injection of OE-Gel through a syringe. Scale bar, 1 cm. k) Macro and micro self-healing process (blue: OE-Gel dyed with methylene blue). Scale bar, 1 cm. l) Schematic illustration of the self-healing mechanism for OE-Gel. m) Strain amplitude sweep of OE-Gel with strains ranging from 1% to 180% (G′: storage modulus, G″: loss modulus). n) Rheological behaviors of OE-Gel under alternate steps of strain sweep (G′: storage modulus, G″: loss modulus). Data are means ± SD ($n = 3$). (*$p < 0.05$, **$p < 0.01$, ***$p < 0.001$).

2.3. Antibacterial Properties of OE-Gel

The inflammatory phase critically influences the healing rate of skin wounds, and bacterial infection represents a primary factor to exacerbates inflammation.[24] Common pathogens such as *E. coli*, *S. aureus*, and *MRSA* were selected as model organisms to assess the antibacterial efficacy of OE-Gel by measuring OD values of bacterial cultures.[24b,25] Compared with the control group, the EPL and OE-Gel groups exhibited broad-spectrum and efficient antibacterial properties (**Figure 3a**), as observed by the absence of bacterial colonies on the bacterial petri dishes. However, the average bacterial survival ratio of the OHAMA group was 96.32 ± 8.46% (Figure 3c), indicating no antibacterial effect of OHAMA. The Ampicillin group displayed effective antibacterial ability against *E. coli* and *S. aureus* but could not combat *MRSA* infection. These results demonstrated the low drug resistance of EPL as well as OE-Gel.

Microscopic analysis revealed that the bacteria co-cultured with EPL and OE-Gel exhibited disrupted membranes, appearing as collapsed and fused entities (Figure 3d). While bacteria in the control, OHAMA, and Ampicillin groups maintained intact cellular structures with no significant differences. The broad-spectrum and efficient antibacterial effect of OE-Gel is attributed primarily to the antimicrobial peptide EPL, which likely disrupts bacterial cell membranes by neutralizing their negative charge, thereby impairing their transmembrane potential and leading to cell lysis.[25] The slow release of EPL during the degradation of OE-Gel ensured prolonged antibacterial protection throughout the wound healing process (Figure 3b). In addition, the Schiff-base bonds within OE-Gel may trap and mechanically disrupt bacteria, collaboratively leading to their death.

2.4. Isolation and Characterization of MSCs-sEVs

Owing to the non-invasive collection methods (irrespective of ethical concerns) and superior proliferation capacities, human umbilical cord mesenchymal stem cells (HUCMSCs) are preferred for skin repair and regeneration over other sources.[26] Multiple studies have highlighted the therapeutic potential of sEVs derived from HUCMSCs throughout the wound healing process.[9,27] HUCMSC-derived sEVs were thus selected as the therapeutic medicine to facilitate skin wound healing in this study. We cultured HUCMSCs and isolated their sEVs from the cultured supernatants. Then, the sEVs were characterized by nanoparticle tracking analysis (NTA), transmission electron microscopy (TEM), and Western blot (WB). The results of NTA showed a uniform particle size distribution, with an average diameter of 136.9 nm and a measured concentration of 1.53×10^9 particles mL^{-1} (Figure S4, Supporting Information). TEM confirmed the typical round or cup-like morphology of sEVs, averaging ≈ 137.5 nm in diameter (Figure S5, Supporting Information). WB analysis verified the presence of surface markers (typically CD9, Alix, and CD63) of sEVs, and the absence of Calnexin protein on the surface of sEVs was detected too (Figure S6, Supporting Information). The experiments above proved that the sEVs were successfully enriched.

2.5. sEVs Loading and Delivery of OE-sEVs-Gel

First, we synthesized OE-Gel and OE-sEVs-Gel. SEM analysis of both gels revealed a continuous porous structure; the presence of sEVs did not alter the structural integrity of OE-Gel (Figure S7, Supporting Information). The average pore sizes of OE-Gel and OE-sEVs-Gel were respectively calculated to be 76.37 ± 18.41 and 81.22 ± 21.94 µm, aligning with the ideal range of 20–125 µm for skin regeneration in mature mammals.[28] The 3D spatial distribution of sEVs in OE-sEVs-Gel was revealed by immunofluorescence multilayer scanning imaging (**Figure 4a**). The sEVs release kinetics exhibited a pH-dependent mode, which derived from the acid-responsive degradation of the Schiff base in OE-Gel. During 4 days of monitoring, more than 80% of sEVs were released by day 3, which actively contributed to the wound healing process (Figure 4b–d). In short, sEVs were successfully loaded and released from OE-sEVs-Gel continuously, facilitating ongoing therapeutic effects and creating an optimal microenvironment for wound healing.[29]

2.6. Biocompatibility of OE-sEVs-Gel

Biocompatibility is an important prerequisite for any therapeutic agents in clinical applications. We evaluated the biocompatibility of sEVs, OE-Gel, and OE-sEVs-Gel, using CCK-8 and hemolysis assays in vitro. Wound healing mainly depends on the proliferation and migration of fibroblasts and endothelial cells.[1b] Hence, we selected mouse embryonic fibroblasts (MEFs) and human umbilical vein endothelial cells (HUVECs) for the follow-up experiments. CCK-8 showed that there was no significant difference between the control group and other groups after different treatments for 24 h ($P > 0.05$) (Figure 4f,g), which indicated no cytotoxicity of OE-sEVs-Gel. Hemolysis test showed good blood compatibility of OE-sEVs-Gel, as the hemolysis ratios for all the OE-Gel, sEVs, and OE-sEVs-Gel groups were below 5%, significantly lower than those treated by 0.1% Triton X-100 (Figure S8, Supporting Information). These results show that OE-sEVs-Gel displays great biocompatibility and is highly promising for clinical uses.

2.7. In Vitro Facilitation of Proliferation, Migration, and Angiogenesis

In this study, we evaluated the cellular promotion effects of OE-sEVs-Gel using HUVECs and MEFs.[30] First, fluorescence imaging demonstrated the intracellular localization of GFP-tagged sEVs (GFP-sEVs), confirming their uptake by HUVECs (Figure 4e). Subsequently, after co-culturing with different interventions for 48 and 76 h, the cell viability of the sEVs and OE-sEVs-Gel groups was significantly improved compared with the control group ($P < 0.001$), and no marked improvement was observed in the OE-Gel group ($P > 0.05$) (Figure 4f). These results indicated that the sEVs play a crucial role in promoting cell proliferation. The EDU positive percentage represents the cell proliferation activity. As shown in Figure 4h, the EDU incorporation percentage of the sEVs and OE-sEVs-Gel groups exhibited a significant improvement in comparison with the control group ($P < 0.001$),

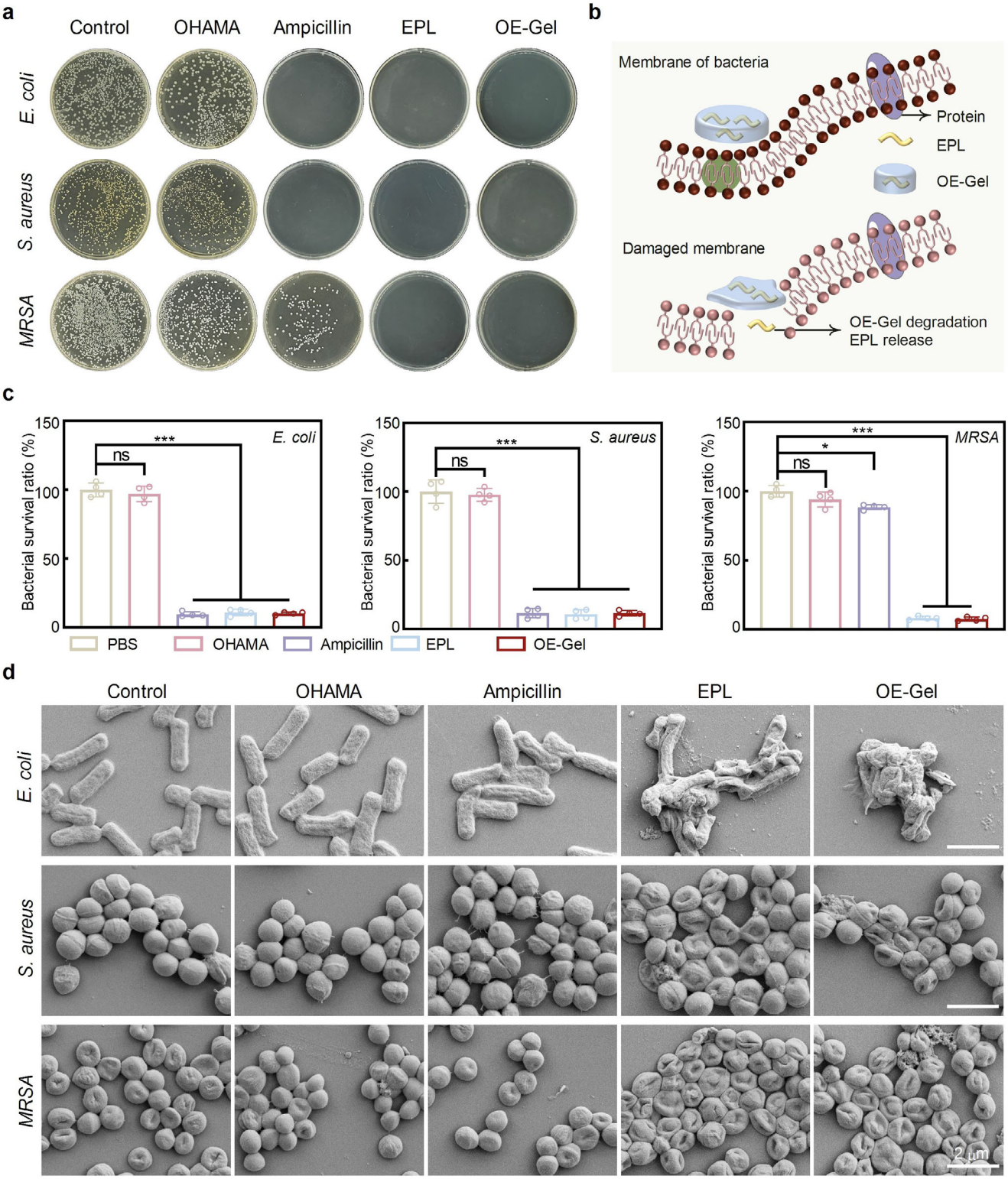

Figure 3. The antibacterial ability of OE-Gel compared with that of OHAMA, ampicillin, and EPL alone. a) Photographs of *E. coli*, *S. aureus*, and *MRSA* colonies after co-culturing with different materials. b) Schematic illustration of the mechanism of antibacterial capability and bacterial membrane destruction induced by EPL release. c) Bacterial survival rate after co-culturing with different materials. Data are means ± SD ($n = 4$). (*$p < 0.05$, **$p < 0.01$, ***$p < 0.001$). d) SEM images of the morphological changes of *E. coli*, *S. aureus*, and *MRSA* after co-culturing with different materials. Scale bar, 2 μm.

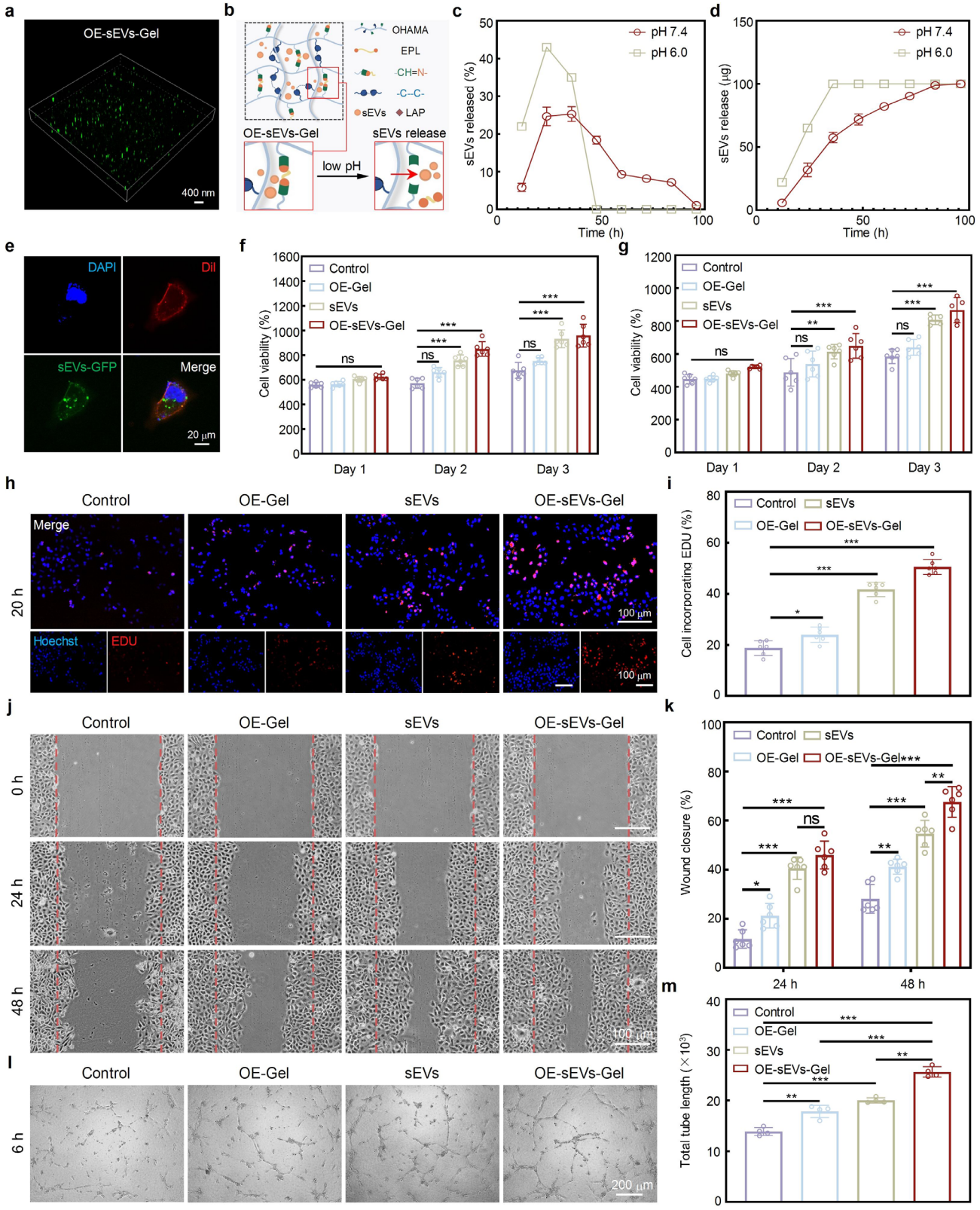

Figure 4. The biological functions of OE-sEVs-Gel. a) 3D fluorescence image of OE-sEVs-Gel. sEVs-GFP: $\lambda ex = 488$ nm, $\lambda em = 525$ nm. Scale bar, 400 nm. b) Schematic illustration of pH-responsive release of sEVs. c) The amounts of released sEVs. d) Cumulative release of sEVs. Data are means ± SD ($n = 3$). e) The phagocytosis assessment of sEVs. DAPI: $\lambda ex = 405$ nm, $\lambda em = 460$ nm. DiI: $\lambda ex = 561$ nm, $\lambda em = 580$ nm. sEVs-GFP: $\lambda ex = 488$ nm, $\lambda em = 525$ nm. Scale bar, 20 μm. f) The CCK-8 assay of HUVECs. Data are means ± SD ($n = 6$). g) The CCK-8 assay of MEFs. Data are means ± SD ($n =$

while the OE-Gel group displayed a slight increase compared with the control group ($P < 0.05$) (Figure 4i). The results of CCK-8 and EDU assays collectively demonstrated the high efficiency of sEVs in promoting cell proliferation.

Cell migration and repair were further assessed through scratch assays. OE-sEVs-Gel showed the highest wound closure rate than the other groups in promoting cell migration over 24 and 48 h (Figure 4j,k). In addition, angiogenesis is a fundamental process in wound healing that entails the formation of tube-like structures by endothelial cells, which progressively extend, branch, and establish interconnected networks.[4a,31] Tube formation capacity was evaluated using HUVECs in vitro (Figure 4l). After 6 h of co-incubation, the OE-sEVs-Gel treated group developed a higher number of branches (Figure S9, Supporting Information) and longer total tube length (Figure 4m) compared with the control group as well as others, indicating the potential of OE-sEVs-Gel in facilitating angiogenesis in vitro.

Fibroblasts play an essential role in the wound healing process, mainly by facilitating collagen deposition, which can establish a stable extracellular matrix scaffold crucial for the formation of new tissues.[32] To assess the impact of OE-sEVs-Gel on MEFs, we performed a series of experiments. CCK-8 showed a significant difference between the control group and the OE-sEVs-Gel group ($P < 0.001$) (Figure 4g), corroborating the effectiveness of OE-sEVs-Gel on MEF proliferation promotion. Images depicted in Figure S10a (Supporting Information) showed a considerable reduction in the residual area after treatment with OE-Gel, sEVs, and OE-sEVs-Gel. The wound closure rates between the OE-Gel group and the OE-sEVs-Gel group were significantly different ($P < 0.001$) (Figure S10b, Supporting Information), indicating the main role of sEVs in promoting cell migration. Taken together, the cell proliferation, migration, and tube formation effectiveness were dominated by sEVs. Meanwhile, OE-Gel exhibited subsidiary effects. All the results indicated that OE-sEVs-Gel may play a pivotal role in promoting wound healing by facilitating cell proliferation and migration, collagen deposition, and blood vessel formation.

2.8. In Vitro Anti-Inflammation of sEVs and OE-sEVs-Gel

To further explore the impact of sEVs and OE-sEVs-Gel on inflammatory responses, Raw264.7 cells were treated with LPS (100 ng mL^{-1}) and then exposed to OE-Gel, sEVs, and OE-sEVs-Gel. ELISA analysis showed that the pro-inflammatory cytokines interleukin-6 (IL-6) and tumor necrosis factor-α (TNF-α) were decreased while the anti-inflammatory cytokine interleukin-10 (IL-10) was increased in both sEVs and OE-sEVs-Gel groups (Figure S11, Supporting Information). In summary, our data indicated that OE-sEVs-Gel had superior therapeutic effects on anti-inflammation by increasing anti-inflammatory cytokines and decreasing pro-inflammatory cytokines.

2.9. In Vivo Analysis of Infected Wound Healing Efficacy

OE-sEVs-Gel exhibited excellent biocompatibility, high antibacterial activity, and sustained sEVs delivery properties, all of which were vital for rapid wound healing, especially for infected wounds.[33] We evaluated the skin wound healing ability of OE-sEVs-Gel using a mouse full-thickness *MRSA*-infected wound model (**Figure 5**a). The macroscopic images of the wound and the corresponding wound fitting pictures at different time points were presented (Figure 5b,c), in which pale yellow pus was observed in the control and sEVs groups due to the bacterial infection on day 3, while the groups with EPL showed no signs of infection, indicating the outstanding antibacterial property of the hydrogel. By day 7, the signs of infection had resolved in the sEVs group but persisted until day 14 in the control group, signifying the great anti-inflammation property of the sEVs. Significantly, the OE-sEVs-Gel group exhibited an enhanced healing rate, particularly during the proliferation phase from day 7 to day 14, with wound closure rates increasing from 48.67% to 92.63%. Macroscopically, the wound was basically covered by newly formed skin on day 14, corroborating the excellent wound repair ability of OE-sEVs-Gel.

To evaluate the therapeutic effectiveness of OE-sEVs-Gel, the tissue samples collected on day 7 and day 14 were analyzed using hematoxylin and eosin staining (H&E) and Masson's trichrome staining (Figure 5f,h). We focused on the skin repair parameters, including epidermal continuity, the number of skin appendages (hair follicles), and collagen deposition. On day 7, the control group displayed an incomplete and discontinuous epidermis and the lowest number of follicles in comparison with other groups, highlighting the significant potential of OE-sEVs-Gel in achieving rapid wound closure and skin appendage formation promotion. On day 14, the OE-sEVs-Gel and sEVs groups exhibited excellent tissue regeneration and hair follicle growth promotion (Figure S12, Supporting Information). Collagen fiber deposition provides a scaffold for tissue regeneration and promotes tissue repair and remodeling. On day 14, the collagen deposition in the OE-sEVs-Gel group was richer than the others, as evident from the intensified blue staining. The collagen volume fraction analysis revealed that the OE-sEVs-Gel group displayed the highest collagen deposition, and the difference is significant ($P < 0.001$) (Figure 5h), confirming high fibroblast promotion ability.

To further investigate the rapid wound healing effects of OE-sEVs-Gel in vivo, we performed and analyzed immunohistochemical (IHC) staining of the skin tissues collected on days 7 and 14. Day 7 is an important turning point between the inflammation stage and proliferation stage, so we used the skin tissue collected on day 7 to analyze the inflammation levels. We assessed the levels of IL-6 and TNF-α, the markers associated with acute inflammation, alongside IL-10, the indicators of inflammation resolution and tissue repair.[34] The control group exhibited a high positive area for IL-6 and TNF-α, signifying severe

6). h) The fluorescence images of the EDU-594 assay of HUVECs. Hoechst 33 342: λex = 346 nm, λem = 460 nm. EDU: λex = 590 nm, λem = 617 nm. Scale bar, 100 µm. i) The percentage of HUVECs that incorporate positive EDU. Data are means ± SD ($n = 6$). j) The bright field images of the scratch assay of HUVECs. The red lines represent the outline before the migration. Scale bar, 100 µm. k) The percentage of the wound closure rate of HUVECs. Data are means ± SD ($n = 6$). l) Bright-field images of the tube formation of HUVECs. Scale bar, 200 µm. m) The total tube length of HUVECs. (The concentration of sEVs in sEVs and OE-sEVs-Gel groups was 30 µg mL^{-1}). Data are means ± SD ($n = 4$). (*$p < 0.05$, **$p < 0.01$, ***$p < 0.001$).

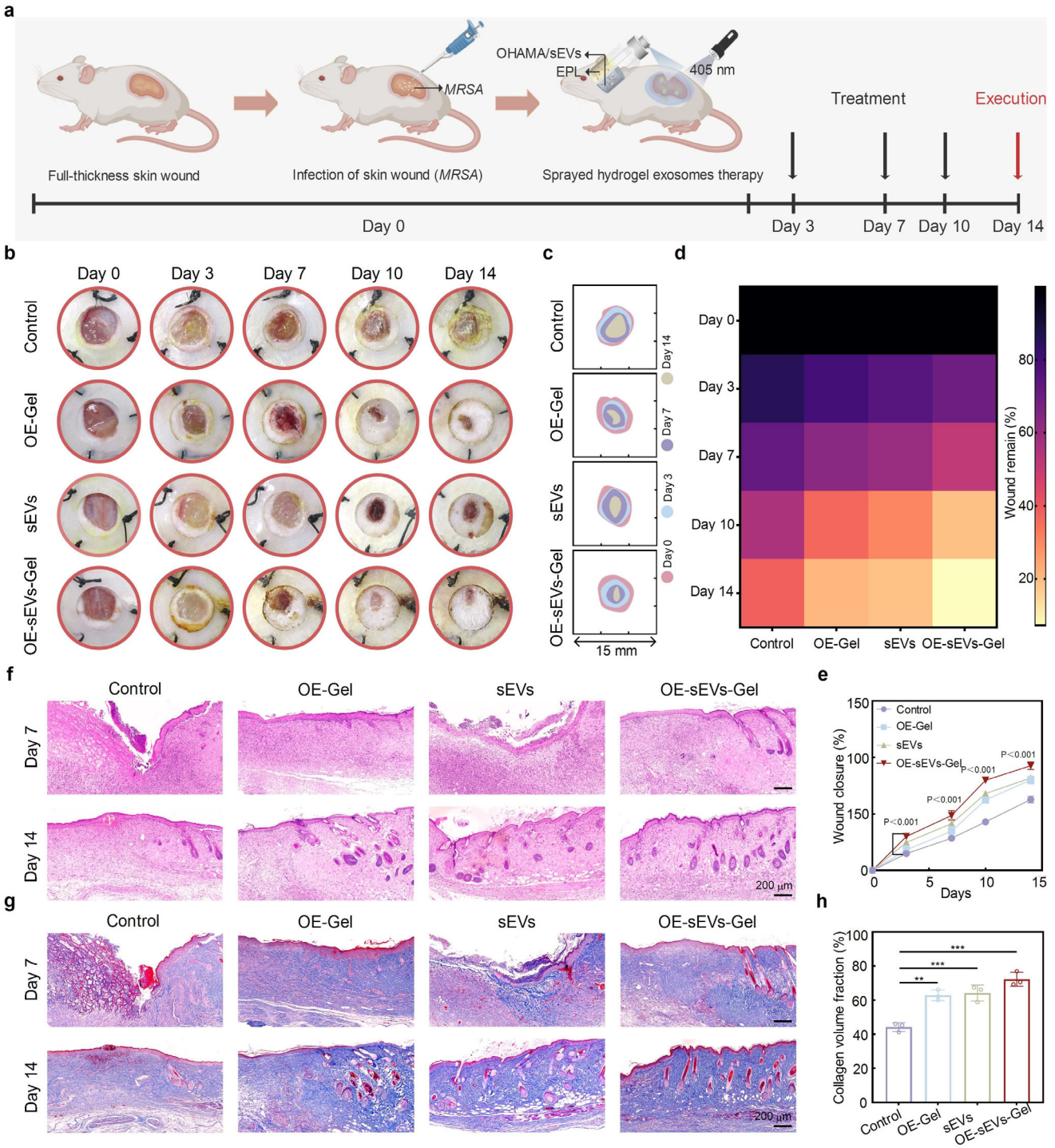

Figure 5. In vivo assessment of antibacterial properties and healing performance of OE-sEVs-Gel. a) Schematic illustration of the *MRSA*-infected wound model and treatment. b) Representative photographs of wound healing after treatment with different dressings (100 μg sEVs each wound in sEVs and OE-sEVs-Gel groups). c) Infected wound closure traces. d) Heat map of wound remaining rate. e) Wound closure rates after treatment with different dressings over time. Data are means ± SD (n = 3). f) H&E staining of the skin tissues after treatment with different dressings on days 7 and 14 (The black arrows represent the hair follicles). Scale bar, 200 μm. g) Masson trichrome staining of the skin tissues after treatment with different dressings on days 7 and 14. Scale bar, 200 μm. h) Collagen volume fraction of the skin tissues after treatment with different dressings on day 14. Data are means ± SD ($n = 3$). ($^*p < 0.05$, $^{**}p < 0.01$, $^{***}p < 0.001$).

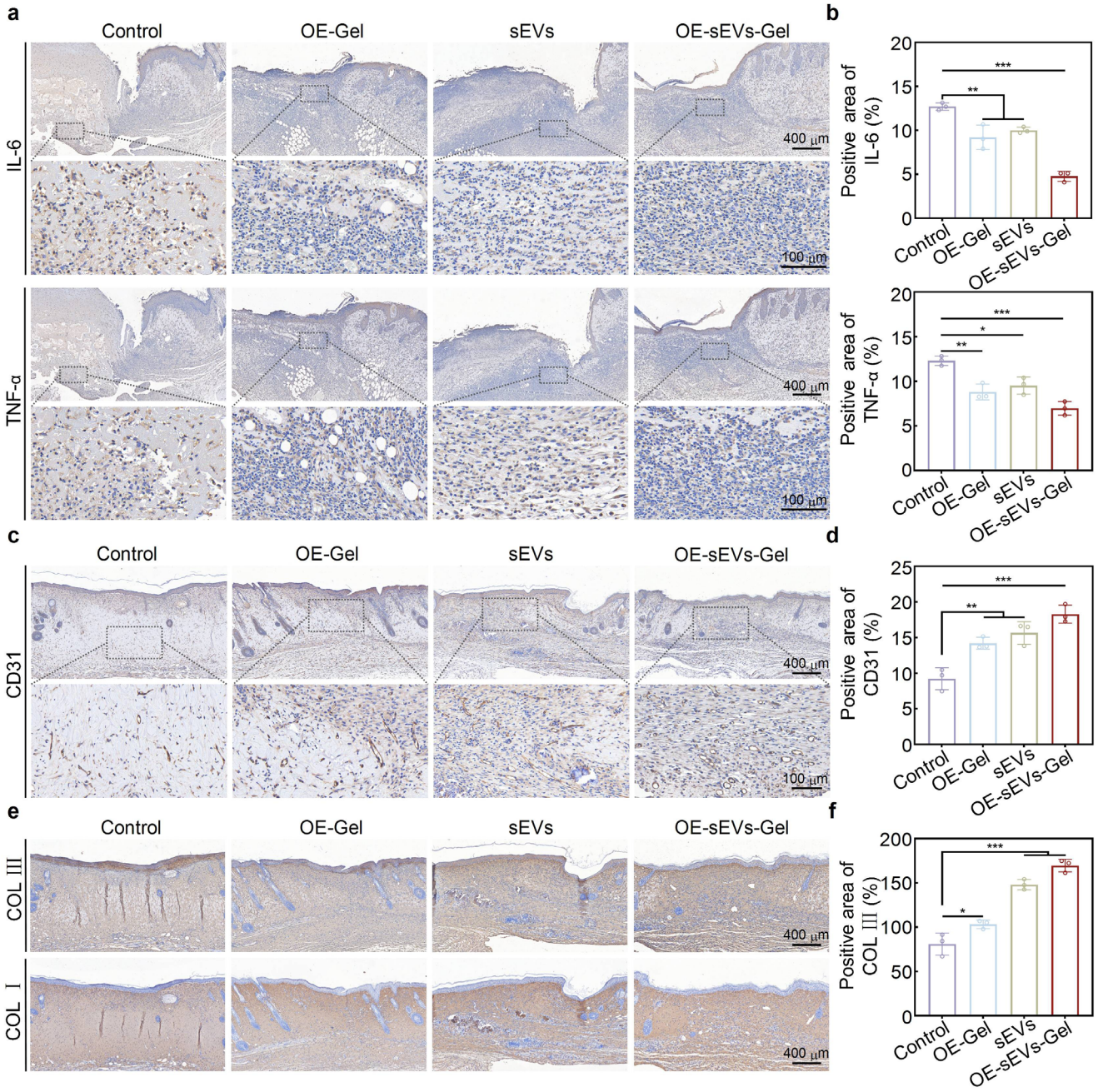

Figure 6. Immunohistochemistry staining of wounds with different treatments. a) IL-6 and TNF-α staining images on day 7. Scale bar, 400 μm. b) Positive area of IL-6 and TNF-α on day 7. Data are means ± SD ($n = 3$). c) CD31 staining images on day 14. Scar bar, 400 μm. d) Quantitative analysis of CD31 of wound tissues on day 14. Data are means ± SD ($n = 3$). e) COL III/COL I staining images on day 14. Scar bar, 400 μm. f) Relative positive area of COL III after different treatments. Data are means ± SD ($n = 3$). (*$p < 0.05$, **$p < 0.01$, ***$p < 0.001$).

inflammation (**Figure** 6a,b). In the OE-sEVs-Gel group, the IL-10 expression level was much higher than that in other groups, suggesting the anti-inflammation effect of OE-sEVs-Gel in vivo (Figure S13, Supporting Information). Meanwhile, fluorescence staining showed the same expression trend, and the anti-inflammatory factors transforming growth factor-β (TGF-β) also exhibited the same expression trend as IL-10 (Figure S14, Supporting Information). Moreover, WB analysis was also conducted to verify the inflammatory state of skin tissues (Figure S15, Supporting Information). The results indicated that the expression of inflammatory factors (IL-6 and TNF-α) was highest in the control group and lowest in the OE-sEVs-Gel group. Meanwhile, the expression of anti-inflammatory factors (IL-10 and TGF-β) was highest in the OE-sEVs-Gel group and lowest in the control group. This was consistent with the outcomes of our immunohistochemical staining and fluorescence staining, demonstrating the potent antibacterial and anti-inflammatory properties of OE-sEVs-Gel.

The inflammatory factors (IL-6, TNF-α) and the anti-inflammatory factors (IL-10, TGF-β) were secreted by M_1 and M_2 macrophages, respectively.[35] To assess the effect of OE-sEVs-Gel on macrophage polarization, the resected tissues were stained by M_1 and M_2 macrophage surface protein markers CD86 and CD206 (Figure S16a, Supporting Information). Notably, the sEVs-treated groups demonstrated higher expression of CD206, highlighting the capacity of sEVs to promote macrophages toward an anti-inflammatory phenotype, the transition from M_1 to M_2 macrophages, thereby enhancing anti-inflammatory factors secretion and curbing excessive inflammation (Figure S16b, Supporting Information). These results demonstrated that OE-Gel could effectively mitigate inflammation by counteracting infections, and the sEVs could ameliorate inflammation by promoting macrophage polarization. The OE-sEVs-Gel would be an efficient antibacterial and anti-inflammatory therapy for infected wound healing.

To verify the cell proliferation of OE-sEVs-Gel, immunofluorescence staining of Ki67 was performed on the skin tissue collected on day 7. As shown in Figure S17 (Supporting Information), the fluorescence intensity of Ki67 in the control group was lower than that in the other groups, while the highest expression level was observed in the OE-sEVs-Gel group, indicating a synergistic effect of OE-Gel and sEVs in promoting cell proliferation. To investigate the angiogenic promotion of OE-sEVs-Gel, the IHC staining of CD31 was performed on the skin tissue collected on day 14. The establishment of a new vascular system is vital for the proliferative phase of wound healing. The IHC results showed that the OE-sEVs-Gel and sEVs groups exhibited higher expression level of CD31 (Figure 6c,d), confirming the potent pro-vascularization capabilities of the sEVs. Therefore, OE-sEVs-Gel could accelerate the formation of skin vessels. Meanwhile, the results of immunofluorescence staining of α-smooth muscle actin (α-SMA)/CD31 were consistent with those of the IHC tests (Figure S18, Supporting Information), which confirm the promoting effect of OE-sEVs-Gel on angiogenesis.

An appropriate collagen deposition can achieve rapid wound healing and optimal healing results.[36] More deposition of Collagen III (COL III) makes the healed skin softer with less or no scar formation.[27b] To evaluate the effects of OE-sEVs-Gel on collagen deposition and scar formation, COL I/COL III IHC staining and immunofluorescence staining were conducted using wound tissues collected on day 14. As shown in Figure 6e,f, the relative positive area of COL III, a critical index for assessing scar formation and repair quality,[26] was higher in the sEVs and OE-sEVs-Gel groups compared to the other groups, confirming the ability of sEVs to promote low-scar healing and favorable healing outcomes of skin wounds. The results of immunofluorescence staining also verified this result (Figure S19, Supporting Information). The ability of collagen synthesis and deposition promotion may be derived from the role of facilitating the proliferation and migration of fibroblasts.

To comprehensively verify the biosafety of OE-sEVs-Gel, H&E staining was performed on visceral slices obtained from the experimental mice following a 14-day treatment cycle (Figure S20, Supporting Information). The results showed that no obvious systemic toxicity occurred in the mice treated with OE-sEVs-Gel compared to the control group, validating the biosafety of OE-sEVs-Gel.

3. Discussion

Full-thickness trauma and infected wounds pose a significant challenge that affects millions of people worldwide, exerting immense pressure on healthcare systems and patients as well.[31] The most common complications associated with these wounds include local or systemic infections, insufficient tissue regeneration, and hypertrophic scars.[37] MSCs-sEVs have emerged as a promising therapeutic agent, offering anti-inflammatory properties and the ability to promote cell proliferation, migration, and angiogenesis in wound healing.[38] However, the presence of infection and the injection procedure can significantly affect their efficacy and delivery performance.

Although the inflammatory response can initiate the process of angiogenesis by releasing cytokines such as TNF-α and IL-6, which promote the proliferation and migration of endothelial cells, persistent inflammation can hinder the normal healing process.[39] During the process of wound healing, infection is the main factor that triggers excessive inflammation. Therefore, infection prevention and excessive inflammation control are crucial for wound healing. Studies have confirmed that the use of hydrogels loaded with sEVs effectively supports the controlled release of sEVs and wound healing.[32] Our research addresses these challenges by proposing a sprayable hydrogel system (OE-Gel), combining the antibacterial properties of OE-Gel with the portability and high efficiency of spray application. It is particularly suitable for irregularly shaped and infected wounds, showing potent broad-spectrum antibacterial effects. Incorporating sEVs into the hydrogel (OE-sEVs-Gel) further enhances the delivery efficiency of sEVs and addresses wound infection and excessive inflammation simultaneously. In the early stage of wound healing, intensified metabolic activity in local tissues produces acidic metabolites, such as lactic acid, and the pH value of the wound microenvironment shifts toward acidity.[40] The acid pH-responsiveness of the hydrogel enables it to rapidly release EPL and sEVs, thereby achieving rapid antibacterial effects and accelerated healing. This OE-sEVs-Gel system not only accelerates the wound healing process but also effectively promotes the formation of COL III, reducing the risk of hypertrophic scarring, thus achieving optimal wound healing outcomes. Moreover, OE-sEVs-Gel exhibits good biocompatibility in vivo, laying a foundation for future applications in clinical wound management.

In summary, our study has successfully developed an sEVs-loaded hydrogel spray that demonstrates significant capabilities in antimicrobial activity, anti-inflammation, tissue regeneration, and scar prevention when applied to infected full-thickness wounds, showing accelerated healing rates and significantly improved healing quality. Our research provides a novel approach for developing wound therapies and sEVs-based formulations. Future studies can focus on targeted sEVs therapies for inflammatory diseases, hair growth promotion, and the mitigation of hypertrophic scars.

4. Conclusion

In our study, we developed a clinically-promising sEVs-loaded dual-network hydrogel spray (namely OE-sEVs-Gel) that consists of EPL, OHAMA, and HUCMSC-derived sEVs for the rapid healing of full-thickness skin wounds. The hydrogel's cross-linking

network, formed by Schiff-base and photo-crosslinked bonds, endows it with properties such as appropriate swelling ability, degradability, injectability, adhesiveness, and self-healing capabilities. In vitro, OE-sEVs-Gel showed strong antibacterial activity and sustained sEVs release without compromising their biological activity. In vivo, it provided continuous therapeutic benefits, including anti-inflammation, cell migration and proliferation, angiogenesis, collagen deposition, and prevention of hypertrophic scarring. Overall, our hydrogel system, designed for sustained sEVs release, proved safe and effective for treating infected wounds, presenting a new strategy for wound care and sEVs-based treatments.

5. Experimental Section

Materials: Sodium hyaluronate (Mw 200000-400000, H74483-100g, ACMEC, Tianjin, China), Sodium periodate (D54001-25G, Meryer Chemical Technology Company, Shanghai, China), Ethylene glycol (E809056-500ml, Macklin, Shanghai, China), Methacrylic anhydride M-58350, HEOWNS, Tianjin, China), ϵ-Poly-Lysine (E-0150697, HEOWNS, Tianjin, China), LAP (EFL, 85073-19-4, China), and other regents were commercially available and used as received.

Synthesis of OHAMA: OHA was synthesized according to a reported method.[41] Briefly, HA (1.0 g) was dissolved in distilled water (100 mL). Under dark conditions, $NaIO_4$ (0.6 g, 2.8 mmol) was dissolved in distilled water (5 mL), then added drop by drop to the HA solution with constant stirring. The reaction was maintained in darkness at 25 °C for 4 h, and ethylene glycol (1 mL) was added to terminate the reaction. After stirring for 1 h, the mixed solution was dialyzed in deionized water for 3 d, then freeze-dried to obtain OHA. OHAMA was synthesized as previously reported.[16b,42] Briefly, OHA (1.0 g) was dissolved in distilled water (100 mL) and stirred until completely dissolved. Then, methacrylate (2 mL) was added, and the reaction was maintained for 12 h with pH at 8.5 and temperature at 4 °C. Finally, the solution was dialyzed for 3 d and freeze-dried for 2 d. The obtained substances were stored at −20 °C for later use.

Synthesis of Hydrogels: First, EPL (4.8, 5.4, and 6.0 mg) was dissolved in distilled water (1 mL) at room temperature to prepare 4.8%, 5.4%, and 6.0% *w/v* EPL solutions, then adjusted the pH to 8.5. The same mass of OHAMA was dissolved in PBS (1 mL) at room temperature to prepare 4.8%, 5.4%, and 6.0% *w/v* OHAMA solutions, and 2.5% (*w/v*) of the photo-initiator LAP (10 µL) was added to the OHAMA solutions. EPL and OHAMA solutions were placed into two spray bottles for the hydrogel spray fabrication. Finally, the solutions were sprayed simultaneously, and the OE-Gel was formed by exposing the mixture to 405 nm UV light. In addition, the OHAMA hydrogel was only constituted by photo-crosslinking bonds, and the OHA/EPL hydrogel was fabricated by OHAMA and EPL without photo-crosslinking bonds.

Characterization of Hydrogels: First of all, the EPL and OHAMA solutions mentioned before were configured. Solutions were sprayed simultaneously, with 405 nm light used to crosslink the C═C bond, then the gelation time of different hydrogels was observed and recorded. Fourier transform infrared spectroscopy (FTIR) of OHAMA, OHA/EPL hydrogels, and OE-Gel in the range of 4000–500 cm^{-1} was measured on a Fourier Transform Infrared Spectrometer (FTIR Spectrometer, Bruker, TENSOR II, Germany). Freeze-dried hydrogels were sprayed with a thin layer of gold and then subjected to an emission scanning electron microscope (SEM, FEL, Apreo S LoVac, Czech) for observation and photographing. Image J (NIH, Image J v1.54t, USA) was used to measure the pore size of all samples. The experiments were repeated three times. The equilibrium swelling ratio (ESR) of the hydrogel was measured by swelling assay.[43] After fabrication of hydrogels, we gently wiped the surface water with filter paper, weighed and recorded the initial weight W_0, and soaked the hydrogel in PBS at 37 °C. Hydrogels were taken out per 30 min, wiped, weighed, and the weight was recorded again (W_t) until the weight kept constant, which represented that the hydrogel reached expansion equilibrium. ESR is calculated as follows: $ESR\ (\%) = (W_t\text{-}W_0)/W_0 \times 100\%$. The degradation ability of hydrogels was tested by the weighing method.[43] First, the initial weight W_0 of hydrogels was measured and recorded, and then the weight was recorded (W_t) per 12 h. The experiment was carried out for 4 d. The formula for calculating the degradation ratio is as follows: $DR\ (\%) = (W_t\text{-}W_0)/W_0 \times 100\%$.

Characterization of Hydrogel Properties: Injectability characterization required pre-mixing of OHAMA and EPL in equal volumes, and subsequently, the mixture was dyed light blue with methylene blue. Then, the hydrogel was added into a 5 mL syringe, and "HA" was written on paper with the syringe, and took photos for recording. To characterize the self-healing property of the hydrogel. Two hydrogels with a diameter of 10 mm and a height of 4 mm were prepared, and one was stained with methylene blue (transparent blue), while the unstained one showed transparent white, the inherent color of OE-Gel. Then, the hydrogels were cut into two pieces, respectively, and reassembled from the broken ends. Finally, the healing process was observed and photographed at 25 °C. The quantitative test was conducted as follows. The hydrogel was prepared into a cylindrical shape with a diameter of 30 mm and a height of 1 mm. Strain amplitude scanning (γ range 1%–500%, fixed angular frequency 1 rad s^{-1}) was used to determine the critical phase transition stress point. Then, a fixed angular frequency alternate step strain scanning of 1 rad s^{-1} was used to evaluate the shear thinning and self-healing behavior of the hydrogel. Amplitude oscillating strain from γ = 1.0% (80 s) switched to γ = 180% (80 s) and performed 5 cycles.

In vitro antibacterial activity: Single colonies of Staphylococcus aureus (S. aureus, njlezhen, BLGW23123, China), Escherichia coli (E. coli, njlezhen, BLGW23146, China), and methicillin-resistant Staphylococcus aureus (MRSA, BIO SCI, 43 300, China) were cultured overnight at 37 °C in Laura Brentani (LB) broth (Solarbio, L8291-250g, China). The cultured suspensions were centrifuged and re-suspended twice with PBS (5 mL) to remove dead bacteria. Then, the obtained bacterial suspensions were diluted to 1×10^4 CFU mL^{-1} with PBS. 200 µL PBS, 5.47% OHAMA, 20 mg mL^{-1} Ampicillin, 1.53% EPL, and OE-Gel were added into the 48-well plate (n = 4), co-cultured with 200 µL diluted bacterial suspensions. After incubation at 37 °C for 6 h, all the co-cultured liquids were moved into 1.5 mL centrifuge tubes, respectively. 25 µL were dropped on LB solid medium and incubated at 37 °C for 12–20 h, and 100 µL was taken to detect the optical density (OD) value.[25] The formula for calculating the bacterial survival rate is as follows: Bacterial survival ratio (%) = $(OD_{subject} - OD_{control})/OD_{control} \times 100\%$. Subsequently, the remaining co-cultured liquids were centrifuged (3000 × g, 3 min) respectively to collect bacteria. After three times washing with PBS, the bacteria were fixed overnight with 2.5% glutaraldehyde (NJDULY, NPH9003, China) at 4 °C, then centrifuged again to remove impurities. After washing with PBS three times again, the bacteria were dehydrated with gradient ethanol (30%, 50%, 70%, 80%, 90%, 100%) and washed with distilled water. A 10 µL out of each sample was dropped on the silicon chip and dried. Finally, SEM (FEL, Apreo S LoVac, Czech) was used to observe the structure.

Cell Culture: HUCMSCs were purchased from iCell Bioscience (iCell Bioscience, HUM-iCell-e011, China), then the cells were cultured in DMEM (Thermo Fisher Scientific, 11320033, China) supplemented with 20% fetal bovine serum (FBS, Sigma–Aldrich, F0193-500ML, China) and 1% penicillin/streptomycin (Yeasen, 60162ES76, China). HUCMSCs were grown in a CO_2 incubator under 5% CO_2 and 95% humidity at 37 °C. HUCMSCs were sub-cultured when the confluency reached 80%, at the 3rd-8th passages.[44] The culture medium was changed to the serum-free culture medium for 48 h, and at last, the cultured supernatant was collected and stored at −80 °C.

Isolation and Characterization of sEVs: According to the method described before,[45] the collected cell supernatant was taken to centrifuged (10000 × g, 30 min, 4 °C) to remove dead cells and debris. Then, the supernatant was collected, and filter paper with an aperture of 0.22 µm was used for ultrafiltration to remove larger extracellular vesicles. The obtained solution was then centrifuged twice (110000 × g, 70 min, 4 °C), followed by removing the supernatant and re-suspending the remaining sediment in PBS. Finally, the re-suspended solution was centrifuged

(10000 × g, 10 min, 4 °C) to remove the miscellaneous protein and stored in a −80 °C refrigerator for later use. By TEM (JEOL, JEM-1400 Flash, Japan), the morphology of the sEVs was observed. Nanoparticle tracking analysis (NTA, HITACHI, HT7700, Japan) was used to determine the particle size. Western blotting (WB) was used to detect the expression of CD9 (1: 1000, Beyotime, AF1192, China), CD63 (1: 1000, Beyotime, AF1471, China), and Alix (1: 1000, Beyotime, AG4522, China). Concurrently, the expression of the negative protein Calnexin (1:1000, PTM Bio, PTM-20025, China) was also assessed. sEVs protein concentration was tested by a BCA protein assay kit (Beyotime, P0012, China) according to the reagent instructions.

sEVs Loading and Delivery of the OE-sEVs-Gel: For the fabrication of the OE-sEVs-Gel, 100 µg sEVs were added to the OHAMA solution beforehand, and other operations were the same as the production of the OE-Gel. OE-sEVs-Gel was freeze-dried and observed by SEM (FEL, Apreo S LoVac, Czech). In addition, the distribution of sEVs in OE-sEVs-Gel was further observed and photographed by confocal microscopy (Nikon, TI2-E, Japan) using GFP-tagged sEVs (GFP-sEVs). The sustained release of sEVs was performed using a BCA protein assay kit (Beyotime, P0012, China).[46] In short, OE-sEVs-Gel and OE-Gel were added to the 48-well plate ($n = 3$) with 200 µL PBS in each well. 200 µL sample was collected, and the same volume of PBS was added per 12 h for 4 d. Finally, the concentration was measured according to the instructions, and the sEVs release profile was drawn.

Blood Compatibility Test: The blood compatibility of OE-sEVs-Gel was evaluated by hemolysis. After euthanasia and heparin anticoagulation, 2 mL of fresh mouse blood was obtained by cardiac puncture. Subsequently, the obtained blood was centrifuged (1500 × g, 5 min) and washed 3 times with PBS. Then, a 50 µL concentration of 10% red blood cells was exposed to 500 µL of Triton X-100, PBS, sEVs, OE-Gel, and OE-sEVs-Gel. After incubation at 37 °C for 80 min, centrifugation (2500 × g, 5 min) was performed again. Finally, the OD value of the supernatant at 540 nm was measured by the microplate reader (BioTek, Synergy2, American). The positive control was 0.1% Triton X-100, and the negative control was PBS. The formula for calculating hemolysis ratio is as follows: *Hemolysis ratio* (%) = $(OD_{Sample} - OD_{PBS})/ (OD_{Triton} - OD_{PBS}) \times 100\%$.

sEVs Phagocytosis Assessment: Briefly, GFP-sEVs were purified according to the method described in the isolation of sEVs. After incubating with HUVECs for 7 h, the nuclei were stained by 4′,6-diamidino-2-phenylindole (DAPI, Beyotime, C1002, China), while the cell membrane was stained by 1,1′-dioctadecyl-3,3,3′,3′-tetramethylindocarbocyanine perchlorate (DiI, Beyotime, C1991S, China). The fluorescence images were observed and photographed by confocal microscopy (Nikon, TI2-E, Japan).

Anti-Inflammatory Assessment of OE-sEVs-Gel: The RAW264.7 cells were seeded onto a 12-well culture plate at a density of 8×10^4 cells well^{-1} and incubated at 37 °C for 12 h. The medium was replaced with 1 mL DMEM and 100 ng mL^{-1} LPS for 12 h (the control group was replaced with 1 mL DMEM only). Then, the medium was replaced with different interventions for 24 h. Finally, the cell culture supernatant was collected after centrifugation at 1000 rpm for 10 min. Particulates were removed and the assay was carried out immediately. The productions of IL-6, TNF-α, and IL-10 were determined by ELISA (ELK Biotechnology, China).

Cell Viability and Proliferation Assay: Cell Counting Kit-8 (CCK-8, Solarbio, CA1210-500, China) and BeyoClickEdU-594 (EdU-594, Beyotime, C0078L, China) proliferation assays were used to detect cytocompatibility and proliferative ability of the OE-sEVs-Gel. In the beginning, HUVECs and mouse embryonic fibroblasts (MEFs) were seeded into a 96-well plate (3×10^3 cells well^{-1}). After adhesion for 12 h, CCK-8 was added and co-cultured at 37 °C for 60 min according to the specification, and the OD value at 450 nm was measured. After that, the same operations were done respectively after 24, 48, and 72 h. The cell viability is calculated as follows: *Cell viability* (%) = $(A_t - A_0)/ A_0 \times 100\%$. Where A_0 represents the cell viability of day 0, A_t represents the cell viability of days 1, 2, and 3. The proliferation effects of OE-sEVs-Gel on HUVECs were further detected using EdU-594. Simply, HUVECs were seeded into confocal petri dishes (SAINING Biotechnology,1 050 000, China) at a density of 55×10^4 cells well^{-1}, and treated differently after cell adhesion. 20 h later, the cells were stained according to the instructions, the fluorescence images were observed and photographed by confocal microscopy (Nikon, TI2-E, Japan), and the images were analyzed by Image J (NIH, Image J v1.54t, USA).

Scratch Wound Assay: MEFs and HUVECs were inoculated in 6-well plates (4×10^5 cells well^{-1}) and cultured to adhesion. After the confluency reached 80–90%, 200 µL sterile pipette tips were used to make an artificial wound ($\Phi = 0.3$ mm). After washing with PBS, the DMEM containing 0.1% FBS (JYK-FBS-301, INNER MONGOLIA JIN YUAN KANG BIOTECHNOLOGY CO., LTD.) was added instead. 0.1% FBS was used to provide the necessary growth factors and avoid apoptosis, and it has no effect on proliferation at this concentration. The wound was observed and photographed by a microscope (Olympus, CKX53, China) after 0, 24, and 48 h under different treatments, and the data were analyzed by Image J (NIH, Image J v1.54t, USA). The wound healing rate is calculated as follows: *Wound closure* (%) = $(Area_0 - Area_t)/ Area_0 \times 100\%$. Where $Area_0$ represents the scratch area of 0 h, $Area_t$ represents the scratch area of 24, 48 h.

Tube Formation Assessment: The tube formation experiment was carried out with the 3rd-4th passages of HUVECs. 50 µL precooled Matrigel (Beyotime, C0383-5ml, China) was mixed with DMEM medium at a ratio of 1: 1, and then 100 µL of the mixture was uniformly spread on a 96-well plate. The gel was formed at 37 °C for ≈ 60 min. HUVECs were then re-suspended with serum-free DMEM inoculated on the gel (2×10^3 cells per well) and treated with different interventions. After 6 h, a bright field picture was taken using a microscope (Olympus, CKX53, China). Image J (NIH, Image J v1.54t, USA) was used to assess and quantify the number of nudes and the total length of the tube structures.

OE-sEVs-Gel Spray Wound Healing Study In Vivo: The animal experiments were conducted in the Animal Center of the Institute of Radiation Medicine, Chinese Academy of Medical Sciences, all animal testing procedures were in line with the humanitarian spirit and approved by the Institute of Radiation Medicine, Chinese Academy of Medical Sciences (approval number: IRM/2-IACUC-2311-007). 24 female Kunming mice (25–30 g, 5 weeks) were fed for 2 weeks to construct an infected full-thickness skin wound model. In short, after anesthetizing the mice with isoflurane, a full-thickness wound with a depth of 2 mm was made on the back with a 7 mm diameter perforator (3bio, 69038-07, China). Then, customized silicone wound splints with an outer diameter (OD) of 15 mm and an inner diameter (ID) of 9 mm (Hede biotechnology, China) were sewn around the wound to prevent skin contraction, and 10 µL of *MRSA* with a concentration of 1×10^6 CFU mL^{-1} was dropped on the wounds. According to different treatments, experimental animals were randomly sorted into four groups: PBS group, OE-Gel group, sEVs group, and OE-sEVs-Gel group (6 mice in each group, one wound on each mouse); all wounds were covered with commercial dressing (3M, 3582, China). The mice were photographed and changed dressings on days 3, 7, and 10 and were executed on days 7 and 14. Tissues were collected from the wounds and stored in 4% paraformaldehyde (servicebio, G1101-15ML, China) for later testing. The wound area was calculated using Image J (NIH, Image J v1.54t, USA).

Histological and Pre-Healing Factors Analysis: Wound area tissues of each group were acquired during the healing process and analyzed by hematoxylin-eosin (H&E) staining, Masson tri-color staining, immunohistochemical staining, and immunofluorescence staining to determine the morphological changes and pre-healing factor expression during the wound healing process. Samples fixed with 4% paraformaldehyde were embedded in paraffin and dyed with H&E and Masson tri-color according to the manufacturer's manual. Histological images were observed and captured by 3DHISTECH (Pannoramic Scan, Hungary). The number of hair follicles and the collagen fraction were measured by Image J (NIH, Image J v1.54t, USA). Immunofluorescence staining, double immunofluorescence labeling method: CD31/α-SMA, COL I/COL III, and CD86/CD206. Samples with the primary antibody including anti-CD31 (1: 200, HUABIO, M1511-8, China) and anti-α-SMA (1: 200, Affinity, BF9212, UK), anti-COL I (1: 300, Proteintech, 66761-lg, China) and anti-COL III (1: 200, Proteintech, 22734-1-AP, China), anti-CD86 (1: 200, HUABIO, ET1606-50, China) and anti-CD206 (1: 200, HUABIO, HA722892, China) were co-incubated at 4 °C overnight, and then co-incubated with the secondary antibody TRITC (1: 100, Zsbio, ZF-0316, China) and FITC (1: 100, Zsbio, ZF-0312, China)

at 37 °C for 1 h. The nuclei were then stained with DAPI (Solarbio, C0065, China) for 10 min. Immunofluorescent staining includes: IL-6, IL-10, TNF-α, TGF-β. The procedure was similar to that of double staining, the samples correlated with anti-IL-6 (1: 200, HUABIO, EM1701-45, China), anti-IL-10 (1: 200, HUABIO, ER1911-19, China), anti-TNF-α (1: 200, Proteintech, 60291-1-Ig), and anti-TGF-β (1: 100, HUABIO, HA721143, China) were co-incubated at 4 °C overnight, and then combined with the secondary antibody FITC (Anti-rabbit, 1: 100, ABCAM, Ab6717, China) and FITC (Anti-rat, 1: 100, Zsbio, ZF-0312, China) at 37 °C for 1 h. The nuclei were stained with DAPI (Solarbio, C0065, China) for 10 min. Finally, images were captured by 3DHISTECH (Pannoramic Scan, Hungary) and processed by Image J (NIH, Image J v1.54t, USA).

Western Blot Assay of Inflammatory Factors: Western Blot analysis was performed to detect the inflammatory level of skin tissues. Here, skin tissues were collected for subsequent grinding and protein lysis. The protein of each group was normalized (30 µg) and separated by 12% sodium dodecyl sulphate–polyacrylamide gel electrophoresis (SDS-PAGE) and transferred to polyvinylidene difluoride (PVDF) membranes. After 1 h of blocking with 5% non-fat milk in 1 × TBST at room temperature, the membranes were incubated with primary antibodies IL-6 (1: 1000, Beyotime, AF0201, China), TNF-α (1: 1000, ProMab Biotechnologies Inc., 20 161, American), IL-10 (1: 1000, Biodragon, RM5106, China), TGF-β (1: 1000, Beyotime, AF0297, China), and GADPH (1: 1000, Beyotime, AF1186, China) overnight at 4 °C and then were incubated with secondary antibody (1: 1000) for 1 h at room temperature. Eventually, the membranes were washed three times with 1 × TBST and detected by an enhanced chemiluminescence (ECL) system (Beyotime, P0018S, China). Densitometric analysis of Western blot was determined with a gel imager system (Azure, C600, America).

Immunohistochemistry (IHC): Wound area tissues of each group were also analyzed by immunohistochemical staining to determine the morphological changes and pre-healing factor expression during the wound healing process. Specifically, inflammatory factors (IL-6, IL-10, TNF-α), neovascularization (CD31 and α-SMA), and collagen production (COL I and COL III) were observed and calculated using ImageJ.

Data Analysis: Statistical analysis was performed using GraphPad Prism (v9.0). The difference between any two groups was analyzed using a two-tailed unpaired Students' *t*-test. For the comparison of more than two groups, the Tukey multiple comparison univariate ANOVA and Bonferroni post hoc analysis were used. The grouped data were evaluated using Dunnett's bidirectional analysis of variance for multiple comparisons. $P < 0.05$ was considered statistically significant. The data presented were the mean ± SD of at least two independent experiments.

Supporting Information

Supporting Information is available from the Wiley Online Library or from the author.

Acknowledgements

This work was financially supported by the National Natural Science Foundation of China (Grant No. 22425401, 22174072, 82373115, and 82274312) and the Key Projects of Science and Technology in China (Grant No. BKJ21J016a and KJ2023B01096).

Conflict of Interest

The authors declare no conflict of interest.

Data Availability Statement

The data that support the findings of this study are available in the supplementary material of this article.

Keywords

antibacterial hydrogel, hydrogel spray, stem cell-derived sEVs, wound healing

Received: October 23, 2024
Revised: July 8, 2025
Published online:

[1] a) P. Martin, *Science* **1997**, *276*, 75; b) O. A. Peña, P. Martin, *Nat. Rev. Mol. Cell Biol.* **2024**, *25*, 599.
[2] J. Zhang, Y. Zheng, J. Lee, J. Hua, S. Li, A. Panchamukhi, J. Yue, X. Gou, Z. Xia, L. Zhu, X. Wu, *Nat. Commun.* **2021**, *12*, 1670.
[3] a) Q. Huang, Z. Chu, Z. Wang, Q. Li, S. Meng, Y. Lu, K. Ma, S. Cui, W. Hu, W. Zhang, Q. Wei, Y. Qu, H. Li, X. Fu, C. Zhang, *Nat. Commun.* **2024**, *15*, 3904; b) T. Deng, D. Gao, X. Song, Z. Zhou, L. Zhou, M. Tao, Z. Jiang, L. Yang, L. Luo, A. Zhou, L. Hu, H. Qin, M. Wu, *Nat. Commun.* **2023**, *14*, 396.
[4] a) B. Zhang, X. Wu, X. Zhang, Y. Sun, Y. Yan, H. Shi, Y. Zhu, L. Wu, Z. Pan, W. Zhu, H. Qian, W. Xu, *Stem Cells Transl. Med.* **2015**, *4*, 513; b) Y. Bo, L. Yang, B. Liu, G. Tian, C. Li, L. Zhang, Y. Yan, *J. Nanobiotechnol.* **2022**, *20*, 291.
[5] Y. Yaghoubi, A. Movassaghpour, M. Zamani, M. Talebi, A. Mehdizadeh, M. Yousefi, *Life Sci.* **2019**, *233*, 116733.
[6] a) F. Tögel, K. Weiss, Y. Yang, Z. Hu, P. Zhang, C. Westenfelder, *Am. J. Physiol.-Renal* **2007**, *292*, F1626; b) T. Wu, Y. Liu, Y. Cao, Z. Liu, *Adv. Mater.* **2022**, *34*, 2110364.
[7] a) H. Kuang, J. Ma, X. Chi, Q. Fu, Q. Zhu, W. Cao, P. Zhang, X. Xie, *ACS Appl. Mater. Interfaces* **2023**, *15*, 22805; b) C. Liang, S. Gao, J. Gao, Y. Xu, Q. Li, *Sci. Rep.* **2023**, *13*, 18431.
[8] V. Horsley, *Cell* **2020**, *181*, 492.
[9] C. Wang, M. Wang, T. Xu, X. Zhang, C. Lin, W. Gao, H. Xu, B. Lei, C. Mao, *Theranostics* **2019**, *9*, 65.
[10] a) X. Zhao, D. Pei, Y. Yang, K. Xu, J. Yu, Y. Zhang, Q. Zhang, G. He, Y. Zhang, A. Li, Y. Cheng, X. Chen, *Adv. Funct. Mater.* **2021**, *31*, 2009442; b) M. Fan, J. Pi, C. Zou, Y. Jiang, Q. Li, X. Zhang, F. Xing, R. Nie, C. Han, H. Xie, *Bioact. Mater.* **2024**, *38*, 1.
[11] M. Chen, Y. Lu, Y. Liu, Q. Liu, S. Deng, Y. Liu, X. Cui, J. Liang, X. Zhang, Y. Fan, Q. Wang, *Adv. Mater.* **2024**, *36*, 2312559.
[12] Y. Liao, L. Xie, J. Ye, T. Chen, T. Huang, L. Shi, M. Yuan, *Biomater. Sci.* **2022**, *10*, 2759.
[13] Q. Yang, L. Tang, C. Guo, F. Deng, H. Wu, L. Chen, L. Huang, P. Lu, C. Ding, Y. Ni, M. Zhang, *Chem. Eng. J.* **2021**, *417*, 127962.
[14] F. Dosio, S. Arpicco, B. Stella, E. Fattal, *Adv. Drug Deliv. Rev* **2016**, *97*, 204.
[15] a) W. Xu, J. Qian, Y. Zhang, A. Suo, N. Cui, J. Wang, Y. Yao, H. Wang, *Acta Biomater.* **2016**, *33*, 131; b) L. Niu, X.-k. Ouyang, J. Ling, N. Wang, *Int. J. Biol. Macromol* **2024**, *281*, 136395.
[16] a) B. Velasco-Rodriguez, T. Diaz-Vidal, L. C. Rosales-Rivera, C. A. García-González, C. Alvarez-Lorenzo, A. Al-Modlej, V. Domínguez-Arca, G. Prieto, S. Barbosa, J. F. A. Soltero Martínez, P. Taboada, *Int. J. Mol. Sci.* **2021**, *22*, 6758; b) J. Chen, J. Yang, L. Wang, X. Zhang, B. Heng, D. Wang, Z. Ge, *Bioact. Mater.* **2021**, *6*, 1689.
[17] L. Li, N. Wang, X. Jin, R. Deng, S. Nie, L. Sun, Q. Wu, Y. Wei, C. Gong, *Biomaterials* **2014**, *35*, 3903.
[18] P. P. Kalelkar, M. Riddick, A. J. García, *Nat. Rev. Mater.* **2021**, *7*, 39.
[19] a) N. Annabi, D. Rana, E. Shirzaei Sani, R. Portillo-Lara, J. L. Gifford, M. M. Fares, S. M. Mithieux, A. S. Weiss, *Biomaterials* **2017**, *139*, 229; b) L. Li, X. Cheng, Q. Huang, Y. Cheng, J. Xiao, J. Hu, *Adv. Healthcare Mater.* **2022**, *11*, 2201286.
[20] S. Li, M. Pei, T. Wan, H. Yang, S. Gu, Y. Tao, X. Liu, Y. Zhou, W. Xu, P. Xiao, *Carbohyd. Polym.* **2020**, *250*, 116922.

[21] J. Qu, X. Zhao, Y. Liang, T. Zhang, P. X. Ma, B. Guo, *Biomaterials* **2018**, *183*, 185.
[22] Z. Wang, F. Yang, X. Liu, X. Han, X. Li, C. Huyan, D. Liu, F. Chen, *Adv. Mater.* **2024**, *36*, 2313177.
[23] Y. Yang, G. He, Z. Pan, K. Zhang, Y. Xian, Z. Zhu, Y. Hong, C. Zhang, D. Wu, *Adv. Mater.* **2024**, *36*, 2404811.
[24] a) J. Oh, S. Kim, M. Oh, A. Khan, *RSC Adv.* **2020**, *10*, 26752; b) L. Guo, Y. Tang, L. Wang, R. Zhou, S. Wang, H. Xu, X. Yang, J. Zhang, J. Chen, C. Xu, Y. Li, H. Tian, *Adv. Funct. Mater.* **2024**, *34*, 2403188.
[25] S. Wang, H. Zheng, L. Zhou, F. Cheng, Z. Liu, H. Zhang, L. Wang, Q. Zhang, *Nano Lett.* **2020**, *20*, 5149.
[26] Y. Liu, M. Zhang, C. Wang, H. Chen, D. Su, C. Yang, Y. Tao, X. Lv, Z. Zhou, J. Li, Y. Liao, J. You, Z. Wang, F. Cheng, R. Yang, *ACS Nano* **2024**, *18*, 13696.
[27] a) J. Hu, C. Zheng, B. Sui, W. Liu, Y. Jin, *World J. Stem Cells* **2022**, *14*, 318; b) P. Guan, C. Liu, D. Xie, S. Mao, Y. Ji, Y. Lin, Z. Chen, Q. Wang, L. Fan, Y. Sun, *Bioact. Mater.* **2022**, *10*, 145; c) Y. Yang, J. Zhang, S. Wu, Y. Deng, S. Wang, L. Xie, X. Li, L. Yang, *Biomaterials* **2024**, *308*, 122558.
[28] J. L. Drury, D. J. Mooney, *Biomaterials* **2003**, *24*, 4337.
[29] Y. Zhang, M. Li, Y. Wang, F. Han, K. Shen, L. Luo, Y. Li, Y. Jia, J. Zhang, W. Cai, K. Wang, M. Zhao, J. Wang, X. Gao, C. Tian, B. Guo, D. Hu, *Bioact. Mater.* **2023**, *26*, 323.
[30] S. Zhang, S. J. Chuah, R. C. Lai, J. H. P. Hui, S. K. Lim, W. S. Toh, *Biomaterials* **2018**, *156*, 16.
[31] X. Han, C. Saengow, L. Ju, W. Ren, R. H. Ewoldt, J. Irudayaraj, *Nat. Commun.* **2024**, *15*, 3435.
[32] H. Peng, H. Li, X. Zhang, J. Tang, Y. Liang, L. Qiao, Y. Zhu, M. Hou, S. Wei, Z. Zhang, C. Liu, X. Li, B. Liang, B. Song, B. Guo, J. Zhang, *Chem. Eng. J.* **2023**, *475*, 146238.
[33] L. Zhou, H. Zheng, Z. Liu, S. Wang, Z. Liu, F. Chen, H. Zhang, J. Kong, F. Zhou, Q. Zhang, *ACS Nano* **2021**, *15*, 2468.
[34] S. A. Eming, T. Krieg, J. M. Davidson, *J. Invest. Dermatol.* **2007**, *127*, 514.
[35] Y. Zhang, D. Liu, W. Chen, Y. Tao, W. Li, J. Qi, *Adv. Mater.* **2024**, *36*, 2409661.
[36] G. C. Gurtner, S. Werner, Y. Barrandon, M. T. Longaker, *Nature* **2008**, *453*, 314.
[37] M. E. Al-Masawa, M. A. Alshawsh, C. Y. Ng, A. M. H. Ng, J. B. Foo, U. Vijakumaran, R. Subramaniam, N. A. A. Ghani, K. W. Witwer, J. X. Law, *Theranostics* **2022**, *12*, 6455.
[38] a) L. J. Born, K. H. Chang, P. Shoureshi, F. Lay, S. Bengali, A. T. W. Hsu, S. N. Abadchi, J. W. Harmon, S. M. Jay, *Adv. Healthcare Mater.* **2021**, *11*, 2002070; b) Y. Li, Z. Zhu, S. Li, X. Xie, L. Qin, Q. Zhang, Y. Yang, T. Wang, Y. Zhang, *J. Nanobiotechnology* **2024**, *22*, 398.
[39] N. Pacienza, R. H. Lee, E.-H. Bae, D.-k. Kim, Q. Liu, D. J. Prockop, G. Yannarelli, *Mol. Ther. Methods Clin. Dev* **2019**, *13*, 67.
[40] a) T. Cui, J. Yu, C. F. Wang, S. Chen, Q. Li, K. Guo, R. Qing, G. Wang, J. Ren, *Adv. Sci.* **2022**, *9*, 2201254; b) X. Liu, G. Dou, Z. Li, X. Wang, R. Jin, Y. Liu, H. Kuang, X. Huang, X. Yang, X. Yang, S. Liu, M. Wu, H. Guo, F. Ding, H. Xu, S. Liu, Y. Jin, K. Xuan, *Adv. Sci.* **2022**, *9*, 2105650.
[41] L. Lei, R. Cong, Y. Ni, X. Cui, X. Wang, H. Ren, Z. Wang, M. Liu, J. Tu, L. Jiang, *Adv. Healthcare Mater.* **2023**, *13*, 2302551.
[42] K. A. Smeds, M. W. Grinstaff, *J. Biomed. Mater. Res.* **2001**, *54*, 115.
[43] L. Qiao, Y. Liang, J. Chen, Y. Huang, S. A. Alsareii, A. M. Alamri, F. A. Harraz, B. Guo, *Bioact. Mater.* **2023**, *30*, 129.
[44] J. Cai, J. Wu, J. Wang, Y. Li, X. Hu, S. Luo, D. Xiang, *Cell Biosci.* **2020**, *10*, 69.
[45] T. Hua, M. Yang, H. Song, E. Kong, M. Deng, Y. Li, J. Li, Z. Liu, H. Fu, Y. Wang, H. Yuan, *J. Nanobiotechnol.* **2022**, *20*, 324.
[46] Y. Liang, M. Li, Y. Yang, L. Qiao, H. Xu, B. Guo, *ACS Nano* **2022**, *16*, 3194.